

## **Chapter 22 – INSPECTION OF HELICOPTER ROTOR BLADES BY NEUTRON- AND X-RAY RADIOGRAPHY**

**M. Balaskó and L. Horváth**  
MTA KFKI Atomic Energy Research Institute  
Budapest  
HUNGARY

### **22.1 INTRODUCTION**

In order to detect the presence of defects in the composite structure of helicopter rotor blades, combined neutron- and X-ray radiography investigations were performed at the Budapest Research Reactor. The rotor blades were about 10 m (or 6,5 m) long, and therefore the images were taken in several segments, and a special program was developed to reconstruct the entire radiographic image from the individual segments. Several types of defects were discovered using neutron radiation: imperfections in the honeycomb structure, resin-rich or resin-starved areas at the core-honeycomb surfaces, in-homogeneities in the adhesive filling, corrosion products behind the covering, and water percolation at the sealing interfaces of the honeycomb sections. The location and condition of structural metal parts was analysed by X-ray radiography.

A comment was once made that a helicopter was a multiple-spindle Wöhler fatigue machine. Although this is perhaps a rather unkind remark there is, nevertheless, some truth in the fact that a helicopter, by its very nature, generates large dynamic forces in its entire rotor system. Basically four constant forces are served by the rotor blades:

- Centrifugal forces;
- Lift forces;
- Flapping moment, i.e., a bending moment about horizontal axis; and
- Drag (or lag) moment, i.e., a bending moment about a vertical axis.

In addition, the rotor blades are used and stored on the airfield during both summer and winter. Altogether the huge loading and the harmful consequences of the weather reduce the life-time of the helicopter rotor blades.

The safe life testing of rotary wing aircraft is of paramount importance and especially as it applies to the rotor blades. The identification of a structural defect that can grow to the point where structural integrity is affected comprises a central challenge. In this process, the inspection of structures and the monitoring of the rate of growth of defects in relation to the total flight hours are essential. The above demands underline the necessity of testing and applying new Non-Destructive Testing (NDT) methods for inspection in service.

### **22.2 METHODS**

Neutron- and X-ray Radiography (NR and XR) utilize transmission of radiation to obtain information on the structure and/or inner condition of a given object. The basic principle of radiography is very simple [1]. The object under examination is placed in the path of the incident radiation, and the transmitted radiation is detected by a two-dimensional imaging system, as illustrated in Figure 22-1. The radiography arrangement consists of a radiation source, a pin hole type collimator which forms the beam, and a detection system which registers the transmitted image of the investigated object.

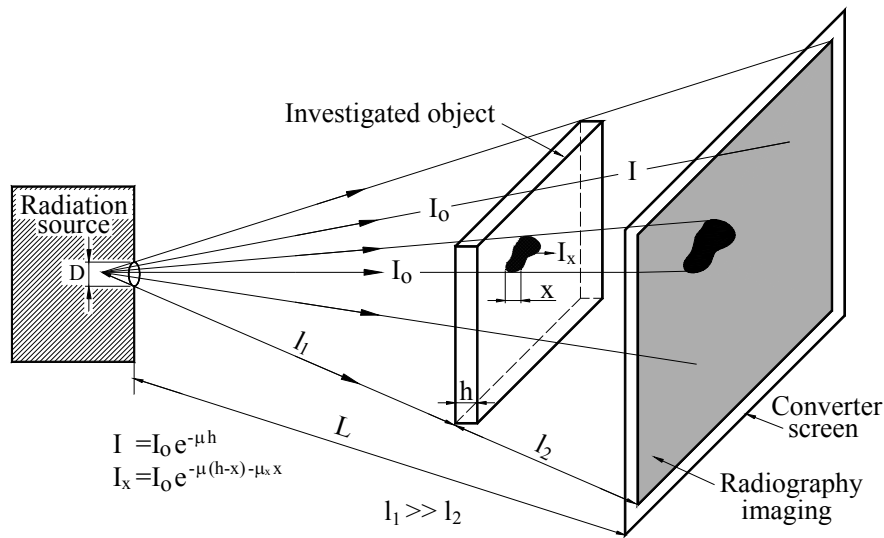


Figure 22-1: General Principle of Radiography.

The most important characteristic technical parameter of a radiography facility is the collimation ratio  $L/D$  where  $L$  is the distance between the incident aperture of the collimator and the imaging plane,  $D$  is the diameter of the aperture. This important parameter describes the beam collimation and will limit the obtainable spatial resolution by the inherent blurring independently from the properties of the imaging system. This unsharpness  $U_{beam}$  can be related to the distance between the object and the detector plane  $l_2$  and to the  $L/D$  ratio:

$$U_{beam} = \frac{l_s}{L/D}$$

Two opposing demands have to be taken into consideration when planning a radiography arrangement: if  $L/D$  is large then the neutron flux  $\Phi_{NR}$  at the imaging plane is relatively weak but the geometrical sharpness is high, and vice versa:

$$\Phi_{NR} = \frac{\Phi_s}{16(L/D)^2}$$

where  $\Phi_s$  is the incident neutron flux.

In radiography imaging the attenuation coefficient  $\mu$  is a crucial parameter. The transmitted intensity of the radiation,  $I$ , passing through a sample with an average transmission of  $\mu$  can be written as:

$$I = I_0 e^{-\mu h}$$

where  $I_0$  is the incident intensity and  $h$  is the thickness of the sample in the beam direction. If there is any inclusion (in-homogeneity, inner structure) in the sample of thickness  $x$  and transmission  $\mu_x$  then the transmitted intensity,  $I_x$  is given as:

$$I_x = I_0 e^{-\mu(h-x) - \mu_x x}$$

If the value of  $\mu$  and  $\mu_x$  are different from each other then the presence of the inclusion will provide a contrast in the radiography image (dark spot in Figure 22-1).

The attenuation coefficient vs. atomic number is plotted in Figure 22-2 for neutron radiation and for gamma- and X-rays. Its value depends on both the coherent and incoherent scattering and on the absorption properties of the element(s). For neutrons  $\mu$  does not show any regularity as a function of atomic number, and for some of the lightest elements (H, B, Li) the attenuation coefficient is by two orders of magnitude greater than the corresponding parameter for most of the technically important elements, such as Al, Si, Mg, Fe, and Cr. This fact is of practical importance, viz. neutrons penetrate almost all metals used for construction purposes with little loss in intensity; in contrast they are considerably attenuated in passing through materials containing hydrogen, such as water, oil or several types of synthetics. On the other hand, in the case of X-ray and gamma radiation, this dependence may be characterized by more or less continuously increasing curves. This means that the radiation is absorbed to a great extent by heavy elements whereas it penetrates light materials such as hydrogen without significant loss in intensity. These differences for various radiations provide the opportunity to gain complementary information by using all three types of radiation together.

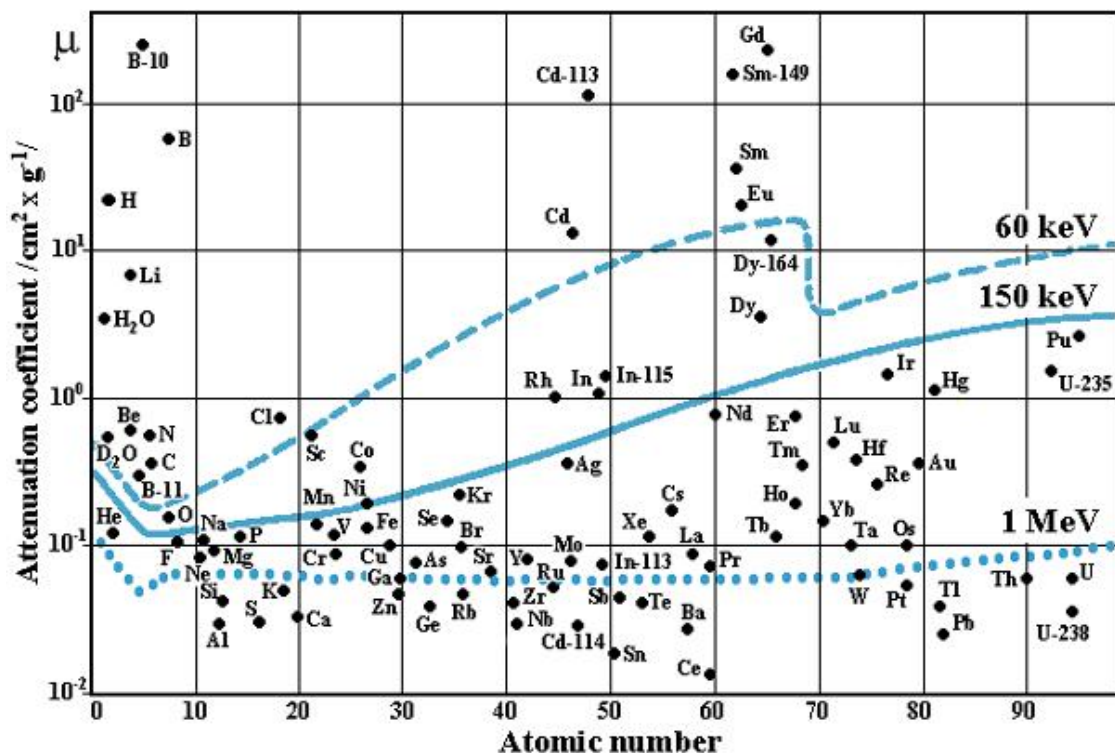


**Figure 22-2: Attenuation Coefficient (note the logarithmic scale) of Elements for Neutrons (separate dots), for 1 MeV Gamma-Ray (dotted line), for 150 keV X-Ray (solid line) and for 60 keV X-Ray (dashed line).**

Our imaging system detects the shading picture of the investigated object by a scintillator screen and a Low-Light-Level (LLL) CCD camera which records the light which is emitted by the scintillator. The images recorded by a CCD camera are inherently digital data and are stored by a PC. A second detection method, an Imaging Plate (IP), was used for the imaging of the plastic fiber-glass rotor blades. The IP is a new film-like radiation image sensor based on photo-excitation luminescence. It consists of a specifically designed composite structure that traps and stores the radiation energy. A polyester support film is uniformly coated with a photo-excitabile luminescent material – barium fluorobromide containing a trace amount of  $\text{Eu}^{2+}$  as a luminescence centre ( $\text{BaFBr} \cdot \text{Eu}^{2+}$ ) and it is then coated with a thin protective layer. The stored energy is stable until scanned with a laser beam whereupon the energy is released as luminescence and detected by a special multiplier. The scanner is read by a PC which provides a visual picture and allows the information to be stored electronically. After scanning and reading the IP plate will be erased prior to reuse.

## 22.3 INVESTIGATED OBJECTS

### 22.3.1 Metal Composite Structure

The majority of the helicopters, Mi-8, Mi-17 and Mi-24 types, in the Hungarian Army's inventory are several decades old and yet they are required to provide continued service. One of the most important components is the rotor blade. They are made of composite structures and contain 21 pieces of honeycomb construction with many bonded surfaces. The 21 sections of the rotor blades were divided into 4 bands horizontally and 53 field columns vertically [4]. A key part of the rotor blade comprises the aluminium alloy main spar bonded to the honeycomb structure as seen in Figure 22-3. Band "A" gives information mainly about the state of the trailing edge and the backside stringer. Band "B" shows the state of the honeycomb structure. The state of the bonded area on the aluminium-alloy spar is represented by band "C". The state of the anti-ice heater and front edge of the rotor blade are both shown by band "D". Every recorded image is identified by a capital letter, indicating the band in the rotor blade, and a two-digit number indicating the field column from which it was taken. These identifiers were used as markers during the inspections. The markers are positioned on the right-upper corner of every exposure.

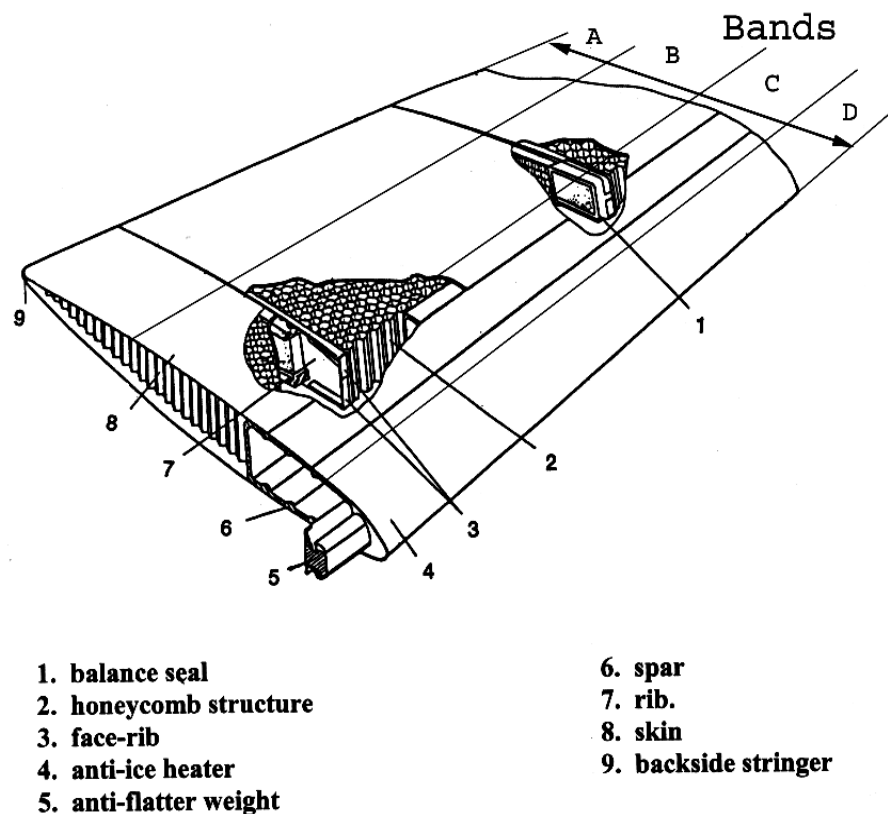
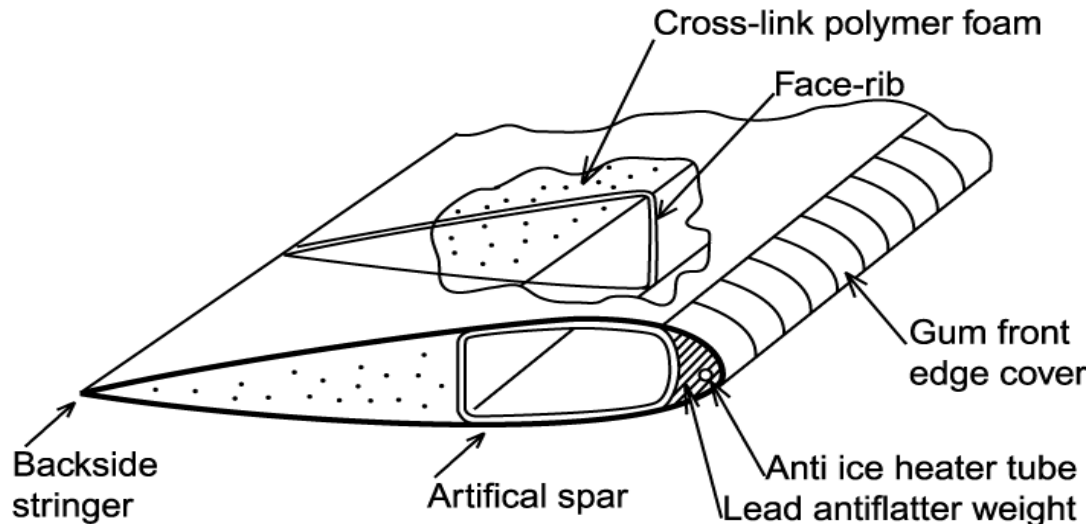


Figure 22-3: The Inner Structure of the Rotor Blade.

### 22.3.2 Plastic Fiber-Glass Structure

The Ka-26 type helicopters were used as reconnaissance-vehicles in the 1980's. Later they were withdrawn from military service and used for agricultural purposes. The rotor blades are made of composite structure except for the root-structure and the anti-flutter weight. The length of the rotor blade is ~ 6.5 m and its weight is ~11.5 kg. The 14 sections of the rotor blades were divided into 2 ("C" and "B") bands horizontally and 38 field columns vertically. Band "B" gives information mainly about the

state of trailing edge and the backside stringer. The state of the bonded area on the plastic fiber-glass spar is represented by band "C" with the anti-flutter weight and the anti-ice heater. These sections are filled up by cross-linked polymer foam. The inner structure of the rotor blade is shown in Figure 22-4.



**Figure 22-4: The Inner Structure of the Ka-26 Rotor Blade.**

## 22.4 EXPERIMENTAL FACILITIES

Measurements were performed at the Dynamic Radiography Station (DRS) [2] at the 10 MW research reactor in Budapest. Its main parameters are as follows. The neutron flux is  $10^8 \text{ n} \times \text{cm}^{-2} \text{ sec}^{-1}$ , the collimation ratio (L/D):190, the diameter of the beam: 220 mm. The portable X-ray generator was adjusted to 150 kV and 3 mA. The radiography images were converted to optical images by a ZnS<sub>Ag</sub>/Li<sup>6</sup> scintillation screen (Applied Scintillation Technologies Ltd.) for NR and a ZnS type LGG400 scintillation screen was used for XR. The optical images were detected by a Low Light Level (LLL) CCD camera, which is cooled by a double Peltier system. The pictures were stored and processed by a Pentium II PC using MATROX Pulsar and Image-Pro Plus software. When the IP detector technique is applied the types of the IP plates are ND 20X25 and ND 20X40 sheets. The type of the reader is BAS 2500 and the type of the eraser is 0308.

Figure 22-5 shows the arrangement of the image system used for metal-composite blades in this work. In addition, we have two background TV cameras. One of these allows position control for the rotor blade picture by picture and the other serves as visual verification of the whole procedure. The rotor blades were moved during the experiments by an extraordinary remote control mechanism. Its weight limit was 250 kg. The surface to be scanned measures 9800 x 700 mm<sup>2</sup>. The state of the rotor blades could be examined in dry and wet conditions, thus simulating complicated weather circumstances. Humidity was controlled using a "Moistening Conditioning" module with water supplied by a closed-circuit High pressure water pump system. The procedure is shown in Figure 22-6. The Moistening module is situated in the middle of the picture. The rotor blade is moved from left to right direction. In the first step, both sides of the bands A and B of the rotor blade are injected by two nozzles. In the second step the direction of movement is changed and the bands C and D are wet. After this procedure it is necessary to wait 15 minutes for the drying. The next step involves the XR measurement as shown in Figure 22-7. The portable X-ray generator is to the right of the rotor blade. The LGG 400 scintillation screen and the light shielded tube of the CCD TV camera can be seen on the left side of the picture.



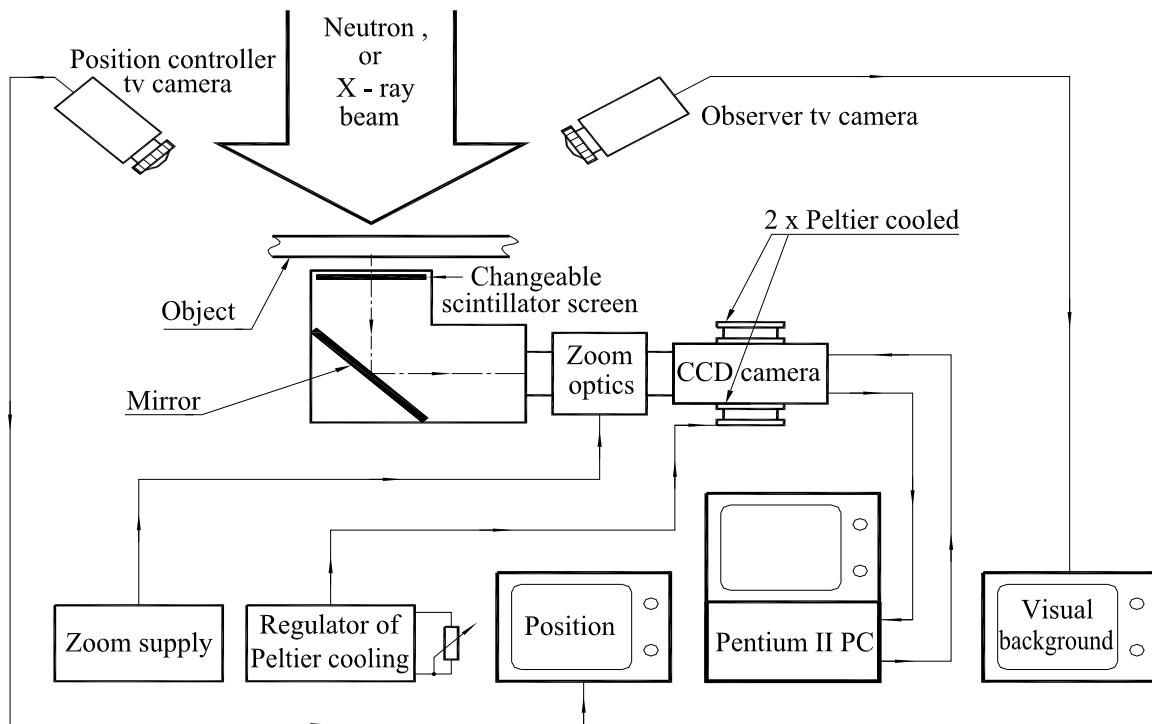


**Figure 22-5: Arrangement of the Imaging System.**



**Figure 22-6: Mi-8 Rotor Blade Undergoing Moisture Conditioning.**

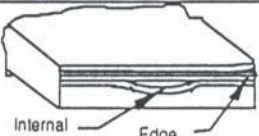
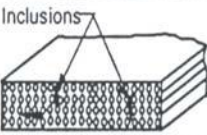
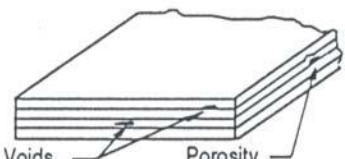
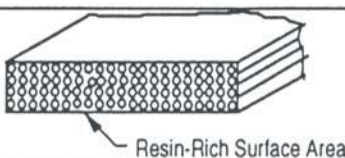
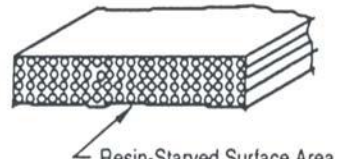
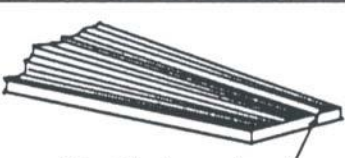
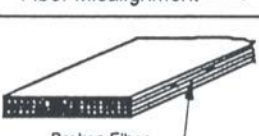
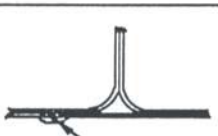


Figure 22-7: Mi-8 Type Rotor Blade Undergoing X-Ray Radiography.

## 22.5 CHARACTERISATION OF THE DEFECTS

Defects can be external or internal to the structure. External defects can be visually inspected, such as dimensions, finish, and warpage. Internal defects of most concern in composites are delaminations, inclusions, voids, resin-rich and starved areas, fiber misalignments, breakages, and de-bonds, as tabulated in Table 22-1. This table also includes illustrations and short descriptions of the defects [3]. Some of the most important and characteristic defects found during this investigation are presented in Table 22-1 using this classification.

**Table 22-1: Descriptions of Defects in Composite Structures.**

Defect	View	Description
1. Delamination		Delaminations are separations within plies of a laminate, and caused by improper surface preparation, contamination and embedded foreign matter.
2. Inclusions		Inclusions are foreign matter embedded in and between laminæ.
3. Voids and Porosity		Voids and porosity are entrapped air and gas bubbles, and are caused by volatile substances, improper flow of resin and unequal pressure distribution. Voids are clustered in the resin, while porosity are pockets within the solid material..
4. Resin-Rich Area		Resin-rich areas are localized, and filled with resin or lacking in fiber. This defect is caused by improper compaction or bleeding.
5. Resin-Starved Area		Resin-starved areas are localized with insufficient resin evident as dry spots, or having low gloss or where fibers are exposed. This defect is caused by improper compaction or bleeding.
6. Fiber Misalignment, Wrinkling, Buckling		Fiber misalignment is a distortion of the plies resulting in changes from the desired orientation, or in fiber wrinkling and buckling. These defects are due to improper lay-up and cure.
7. Fiber Breakage		Broken fibers are discontinuous or misplaced fibers due to improper handling or lay-up.
8. De-bond		De-bonds occur between different details of the built-up structure. Lack of bonding is due to contamination of the surface, excessive pressure or bad fit.

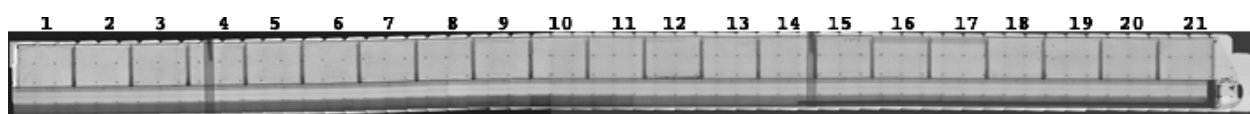
## 22.6 MEASUREMENTS

Strict safety precautions must be followed because of the dangerous nature of the radiations used in the study. In the schedule of inspections the first step was an NR inspection in dry conditions, the second step was the NR inspection in wet conditions, and the third step was the XR test. Twenty-eight pieces of rotor blade were verified by this procedure with no harmful effects on personnel. Because of the large dimensions



of the rotor blades (their length is almost 10 m), it was necessary to investigate the structures in two parts. The first one contains the exposure fields from the end of the blade to the symmetry axis ( $4 \times 27$  pictures). Then the other side of each blade was examined. The second part of the scanning procedure continued to study each blade from the driver end of the symmetry axis ( $4 \times 26$  pictures). The planned exposure field was  $160 \times 140 \text{ mm}^2$ . The simple arrangement of the 212 pictures in 4 horizontal rows and 53 vertical columns would be insufficient for a whole radiographic picture of the rotor blades with good quality. The whole image should have been composed of the small overlapping picture fields, however the fields could not be fitted to each other simply. The re-construction of the whole image was performed on the base of the markers. This procedure consists of two steps. In the first step the positions of the small picture fields were computed on the whole image. The method applied here was successful even when some markers or picture fields were missing. In the second step the whole picture was generated from the small picture fields so that the parts overlapped by two or more fields. Entire radiography pictures are shown in Figure 22-8.

## Section Number:

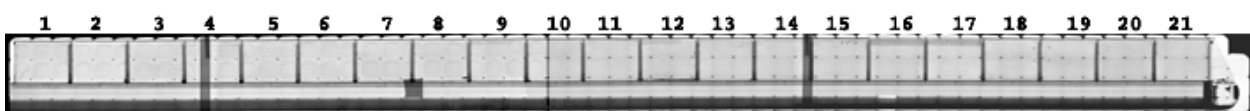


belt

**8/a. Dry NR Whole Picture**

belt

## Section Number:

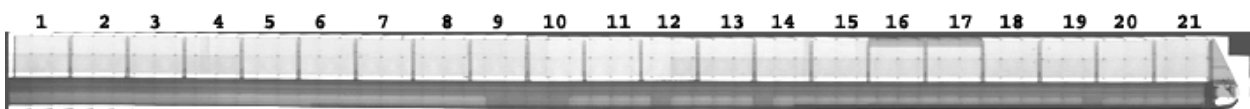


belt

**8/b. Wet NR Whole Picture**

belt

## Section Number:



**8/c. Wet XR Whole Picture**

**Figure 22-8: Radiography Pictures of a Mi-8 Type Helicopter Rotor Blade.**

## 22.7 RESULTS

### 22.7.1 Metal Composite Structure

An important requirement of the radiography inspection was to visualize the resin-rich or resin-starved areas (defect types 4 and 5 in Table 22-1). These types of defects can be identified by the fact that they are clearly visible in the NR images due to the high neutron attenuation coefficient of hydrogen containing materials, while for X-ray radiography they are not visible. This is illustrated in Figure 22-9 which shows a resin-rich area in the honeycomb structure detected by NR. Another interesting point of this image is the well-resolved double contour lines, as they reflect the tilted position of the honeycomb elements.

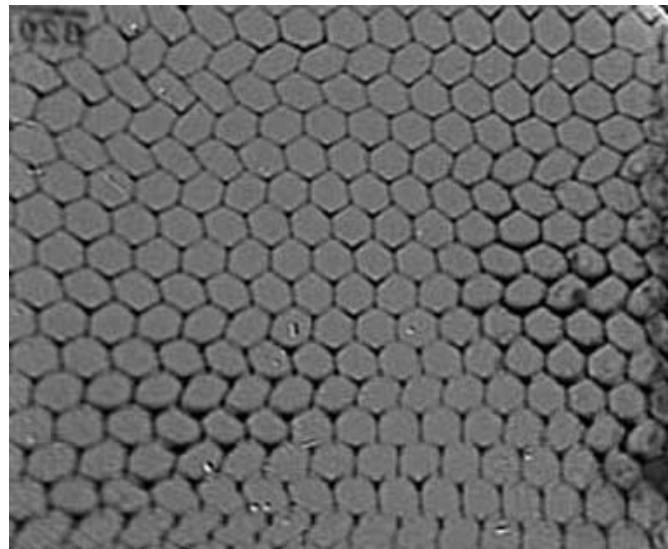
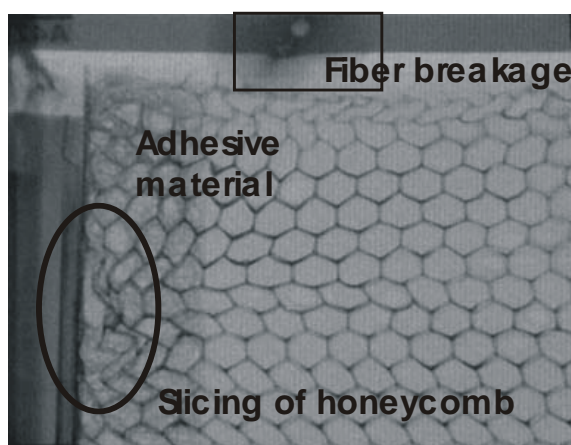
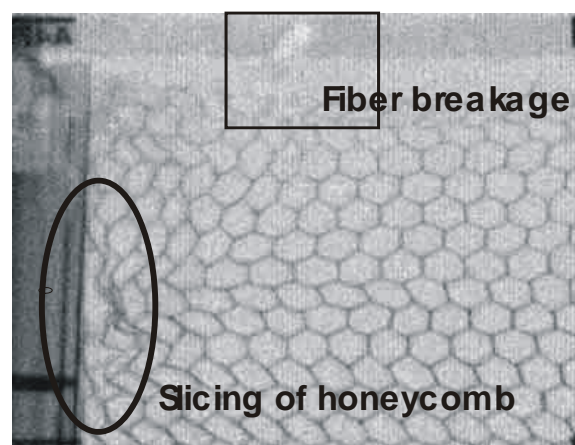


**Figure 22-9: Dry NR Image of the Honeycomb Structure with Resin-Rich Areas (dark spots).**

A fiber breakage (defect type 7 in Table 22-1) in the trailing edge is observable in Figure 22-10. In the same segment another type of defect was detected. Both NR and XR images show slicing of the honeycomb structure near the stiffener, however, the adhesive material can be detected only by NR. One of the most dangerous defects is when a de-bond (defect type 8) in the adhesive surface is present between the honeycomb structure and the aluminium spar. Such observations are illustrated in Figure 22-11. The double contour lines are because of the tilted position of the honeycomb elements. In this investigation one of the most important observations was the presence of cavities, holes and/or cracks in the sealant and at the border of the sections. The problems were caused by water penetrating into these places and freezing which caused damage to the surrounding structure due to the volume expansion of ice. Detection of these defects is very difficult because of the complex arrangement of the composite structure. A combination of ‘dry NR’, ‘wet NR’ and XR experiments made it possible to discover and visualize these defective areas. It was established that the most frequent locations of water penetration were at the border sections or at the honeycomb-adhesive sealant joining surfaces. These defects are visible in Figure 22-12.



**(a)**



**(b)**

**Figure 22-10: (a): Fiber Breakage and Slicing of Honeycomb and the Adhesive Material Revealed by NR; and (b): Fiber Breakage and Slicing of Honeycomb and the Adhesive Material Revealed by XR.**

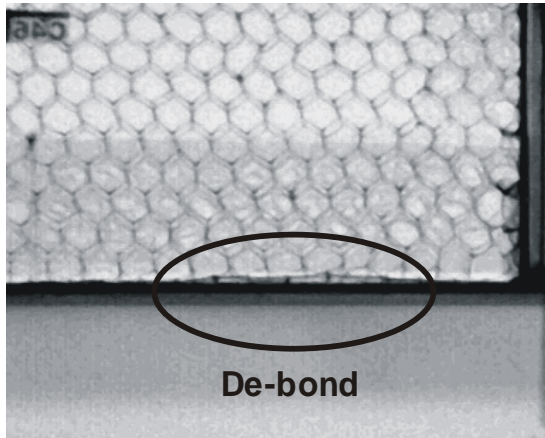


**Figure 22-11: De-Bond in the Adhesive Material Between the Honeycomb and the Aluminium.**

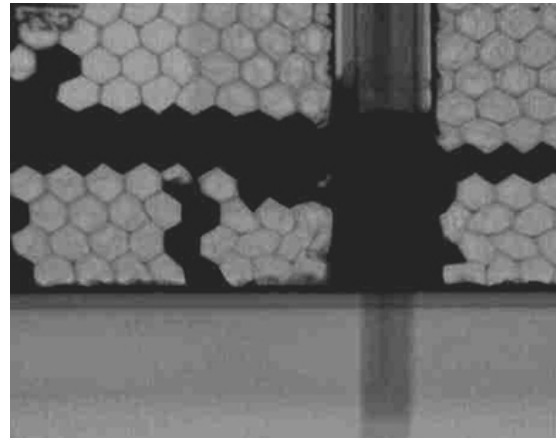


**Figure 22-12: Water Percolation in the Honeycomb Structures by NR.**

Damage caused by splinters may happen during flight missions (defect type 2 in Table 22-1). Our experience showed that such defects occurred during gunnery practice. Although these defects were usually repaired by the maintenance team, a small piece of splinter was not detected by them and thus it was not removed, as may be seen in Figure 22-13(a) NR and Figure 22-13(b) XR pictures. In the NR image the resin rich spots are seen to be as dark as the metal inclusion, while the XR image provides a dark contrast only for heavy elements with large X-ray attenuation.

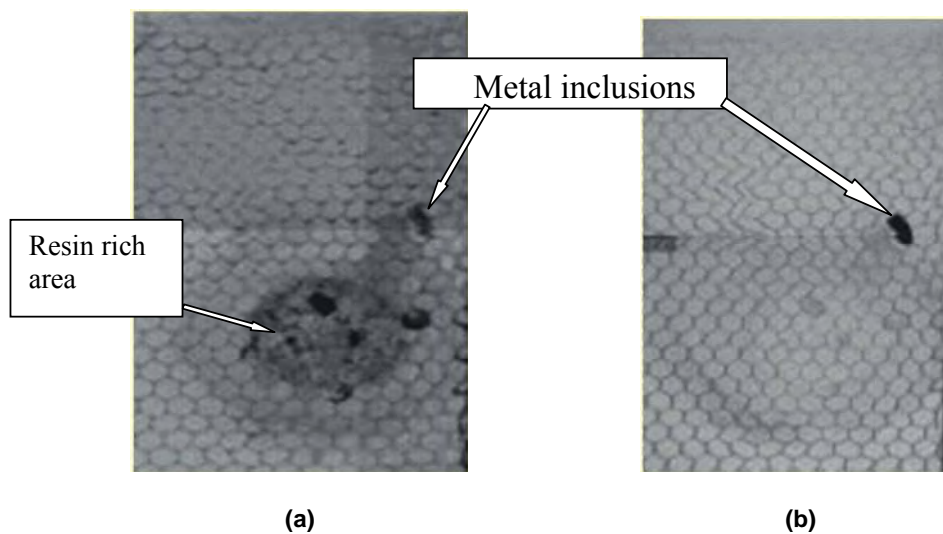


**Figure 22-13: (a) NR Picture of the Repaired Area; and (b) XR Picture of the Repaired Area.**

Corrosion may also cause problems, leading to possible lifetime reductions. Corrosion was detected in some of the investigated blades inside the rotor blade tail element, as shown in Figure 22-14. A resin-rich area is also shown at the bond surface of the honeycomb structure and the last stiffener. X-ray radiography is a complementary and useful tool in assessing the structural integrity of the metal parts of the blades. Figure 22-15 shows the heating element arrangements and their contacts on a blade with some corroded contacts.

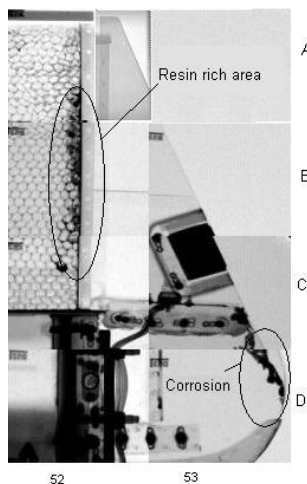


**Figure 22-14: NR Picture of the Corrosion Product in the Tail of the Rotor Blade.**

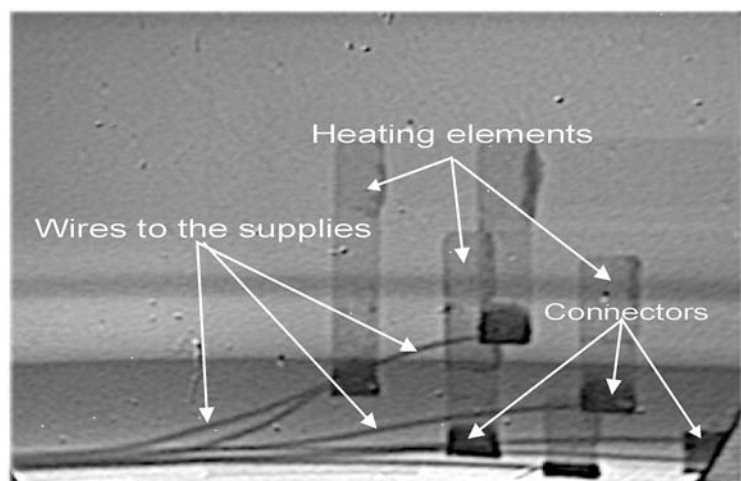


**Figure 22-15: Corroded Heating Elements of the Anti-Ice Heater System Revealed by X-Ray Radiography.**

### 22.7.2 Plastic Fiber-Glass Structure

The customer specified the use of dry state inspections of the rotor blades by neutron and X-ray radiography without inspection in the wet condition. The Imaging Plate (IP) technology, as described previously, was used to record the radiography pictures.

The structure of the plastic fiber-glass rotor blade is very different from the metal composite blade. It contains some metal parts, namely the root structure, anti-flutter weight (iron and lead bar), and some screws and adaptors. Some metal parts are visible in Figure 22-16 but the contrast of the iron and lead bars is not distinguishable by XR. A faint indication is given by the elements of the plastic fiber-glass spar. However many details of the plastic fiber-glass technology are observable in Figure 22-17. Clearly visible is the localization of the sticky material under the closing element of the blade and the border between the sections. It is easy to see that the neutron attenuation coefficient is higher for iron than it is for lead. The two complementary radiography pictures give complete information about the construction of the end element of the rotor blade. Under the blade some beam purity indicators, ASTM sensitivity indicators and step wedge indicators with holes are visible in Figure 22-17. The complementary characteristics of the XR and NR are documented in Figure 22-18 and Figure 22-19. The first one shows the perfect arrangement of the protecting aprons for the front edge. One may postulate that the form of the lead bar anti-flutter weight is intact under the protecting aprons. But this was not true because the materials of the lamination technology destroyed the lead bar. The surface of the lead bar appeared similar to the corrosion products as seen Figure 22-19. In order to study the quality of the fiber-glass bundles of the spar it was necessary to reduce the power of the X-ray generator as illustrated in Figure 22-20. In this figure one may see the perfect arrangement of the bundles. However the authors have no information about the bonding between the plastic fiber-glass spar and the cross-link polymer foam of the section.



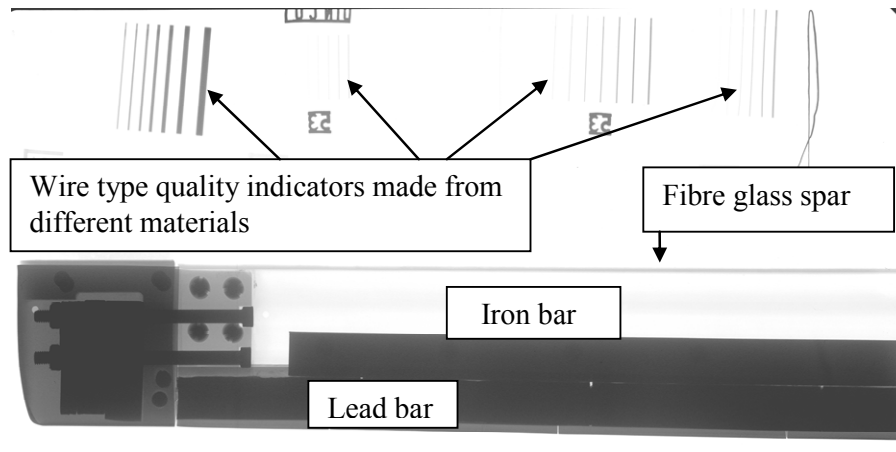


Figure 22-16: End Element of the Ka-26 Helicopter Rotor Blade by XR.

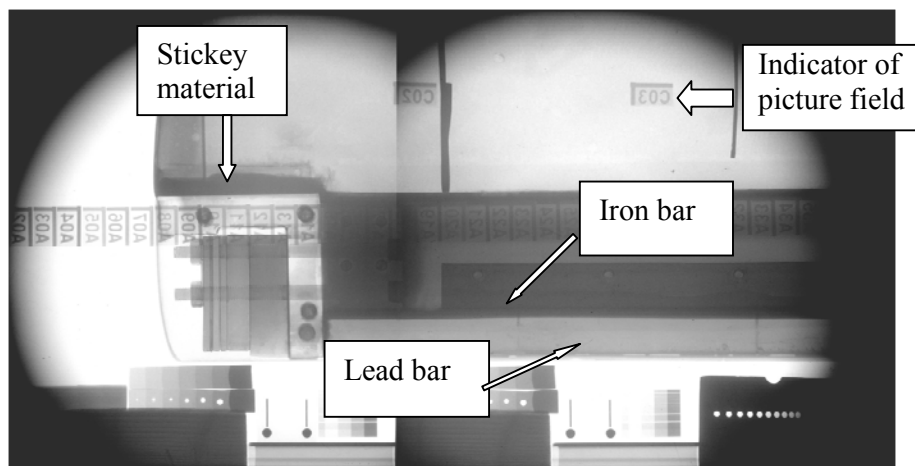


Figure 22-17: End Element of the Ka-26 Helicopter Rotor Blade Revealed by NR.

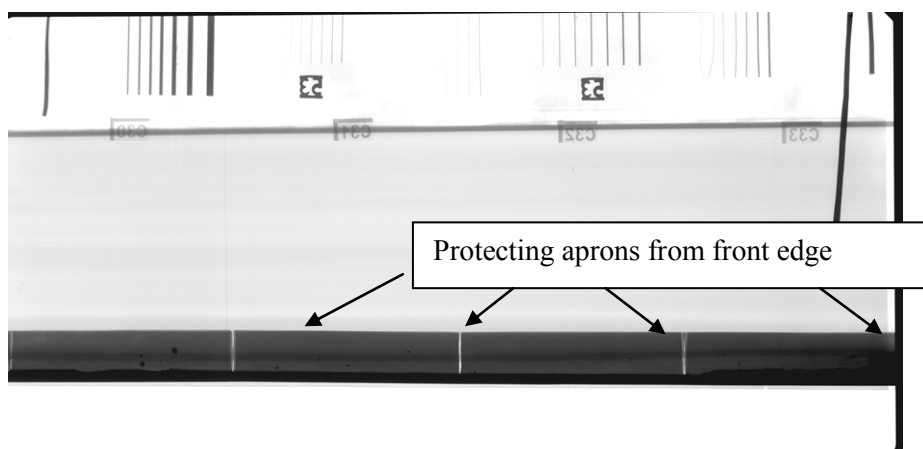
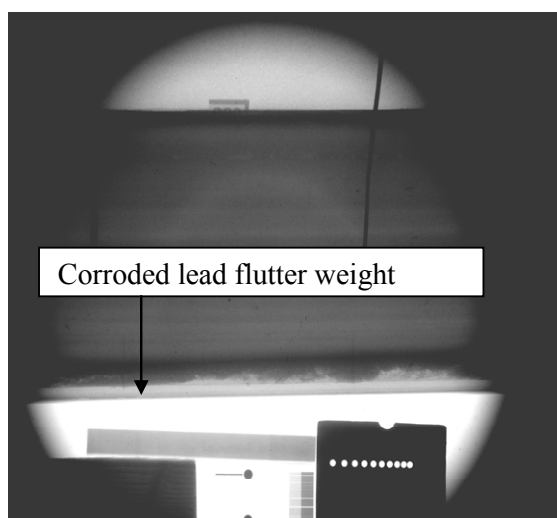
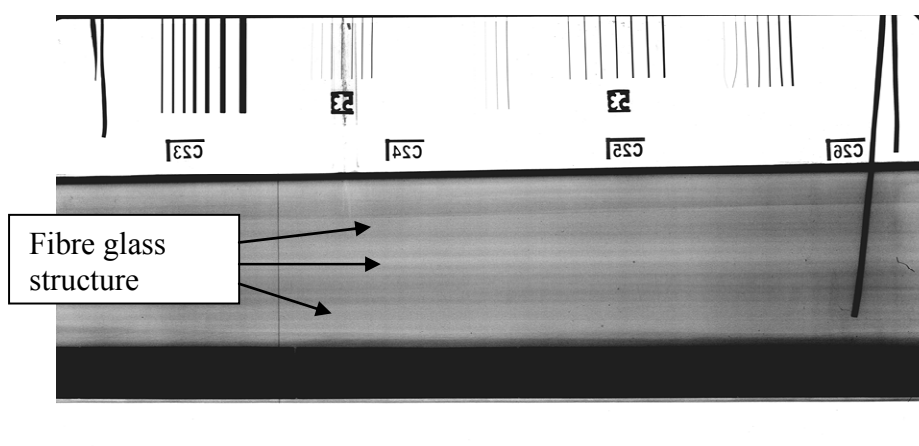


Figure 22-18: Front Edge of the Ka-26 Helicopter Rotor Blade Revealed by XR.



**Figure 22-19: Front Edge of the Ka-26 Helicopter Rotor Blade Revealed by NR with Corrosion Products on the Anti-Flutter Weight.**



**Figure 22-20: Spar in the Middle Part of the Ka-26 Helicopter Rotor Blade Revealed by XR.**

The NR picture of Figure 22-21 shows two areas of de-bond between the spar and the section. In addition one can see an unequal distribution of the sticky material on the lead anti-flutter weight at the front edge of the rotor blade.

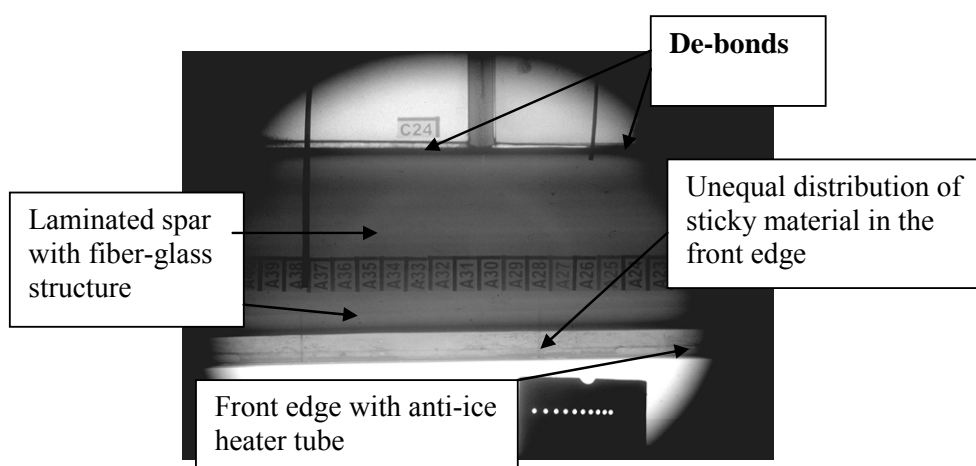


**Figure 22-21: Spar in the Middle Part of the Ka-26 Helicopter Rotor Blade  
Revealed by NR with De-Bonds Between the Spar and the Sections.**

## 22.8 CONCLUSIONS

This investigation revealed no really harmful effects on the helicopter rotor blades using the inspection technology. The most important points of the study were the visualisation of the possible imperfections in the honeycomb structure such as:

- Inhomogeneities of the resin materials (resin-rich or resin-starved areas) at the core-honeycomb surfaces;
- Defects at the adhesive filling (de-bond);
- Water percolation at the sealing interfaces of the honeycomb sections;
- Quality control of resin-rich repaired areas;
- Verification of the positions of metal parts (inclusions) by X-ray;
- Study the condition of the fiber-glass structure in the spar; and
- Verification of the ingress of water into the honeycomb structure and the consequent corrosion of adjacent metal structure.

## 22.9 REFERENCES

- [1] Domanus, J.C., "Practical Neutron Radiography", Ed. J.C. Domanus et al., Kluwer Academic Publ., Netherlands, 1992.
- [2] Balaskó, M. and Sváb, E., "Dynamic Neutron Radiography Instrumentation and Applications in Central Europe", Nucl. Instr. and Methods in Physics Research A377, pp. 140-143, 1996.
- [3] Sem, J.K. and Everett, R.A., "Structural Integrity and Aging Related Issues for Helicopters", RTO/ NATO, ISBN 92-837-1051-7, pp. 5.1 – 5.21, 2000.
- [4] Balaskó, M., Endrőczy, G., Veres, I., Molnár, Gy. and Körösi, F., "Research of Extension of the Life Cycle of Helicopter Rotor Blade in Hungary", Proc. NATO Conference of Applied Vehicle Technology Panel (AVT), Manchester, England, October 7-11, RTO-MP079(II), ISBN 92-837-1089-4, pp. 1-16, 2001.

